Magnetospheric field-line resonances: Ground-based observations and modeling

R. Rankin, K. Kabin, J. Y. Lu, I. R. Mann, R. Marchand, and I. J. Rae
Department of Physics, University of Alberta, Edmonton, Alberta, Canada

V. T. Tikhonchuk
Institut de Physique Fondamentale, Universite Bordeaux 1, Gradignan, France

E. F. Donovan
Department of Physics and Astronomy, University of Calgary, Calgary, Alberta, Canada

Received 24 November 2004; revised 28 February 2005; accepted 13 April 2005; published 28 July 2005.

[1] We present theory and ground-based observations of field-line resonances (FLRs) excited in Earth's magnetosphere. Three FLR observations are reported, which correspond to large-scale standing shear Alfvén wave (SAW) oscillations on nightside field lines extending from premidnight to close to dawn. The eigenfrequencies for these events are modeled using a nonorthogonal covariant-contravariant analysis of the ideal magnetohydrodynamic (MHD) equations. This allows us to use a general field-line topology, an example of which is computed using the Tsyganenko 1996 magnetic field model. We show that field-line stretching, along with assumptions regarding the distribution of density along field lines, is sufficient to explain the observed FLR frequencies. Then, we consider dispersive effects operating at the level of the electron inertial scale near the ionosphere or the ion-acoustic gyroradius in the vicinity of the equatorial plane. Specifically, we estimate the spatial saturation widths and phase mixing timescales based on a simple model of dispersive SAWs. By considering a new model for ionospheric Pedersen conductivity modification by field-aligned currents in SAWs and numerical (finite element model) solutions to the reduced MHD equations, we model specific FLR observations in an approximate axisymmetric field topology. We discuss the interplay of linear and nonlinear phase mixing, along with gradients in dispersion and time-dependent losses due to Pedersen conductivity enhancements.

Citation: Rankin, R., K. Kabin, J. Y. Lu, I. R. Mann, R. Marchand, I. J. Rae, V. T. Tikhonchuk, and E. F. Donovan (2005), Magnetospheric field-line resonances: Ground-based observations and modeling, *J. Geophys. Res.*, *110*, A10S09, doi:10.1029/2004JA010919.

1. Introduction

[2] In Earth's magnetosphere, shear Alfvén waves (SAWs) have been studied extensively in part due to the role they play in forming discrete temporally modulated auroral arcs across a range of length and timescales. Observations spanning more than 3 decades [*Samson et al.*, 1971; *Chen and Hasegawa*, 1974] have established a strong correlation between resonant magnetohydrodynamic (MHD) wave activity [*Southwood*, 1974; *Kivelson and Southwood*, 1986] and auroral arcs [*Hasegawa*, 1976; *Goertz*, 1984]. Auroral arcs typically appear as narrow elongated bands of precipitation in the ionosphere during auroral activity [*Akasofu*, 1974]. The associated MHD perturbations can be routinely measured with magnetometer arrays such as the CANOPUS (Canadian Auroral Network for the OPEN Program Unified Study) array in northern Canada [*Rostoker et al.*, 1995]. Discrete arcs have optical signatures in the ionosphere that are associated with the acceleration of electrons parallel to the geomagnetic field. The energy of the precipitating electrons ranges typically from a few hundred eV to a number of keV. The mechanisms responsible for this acceleration are still a subject of some debate. Possibilities include quasi-static potential structures related to mirroring magnetospheric particle populations [*Chui and Schultz*, 1978; *Knight*, 1973] or small-scale SAWs with transverse (to the magnetic field) scales on the order of the ion gyroradius or electron inertial length [e.g., *Hasegawa*, 1976; *Wei et al.*, 1994].

[3] There are many characteristic scales associated with discrete arcs, ranging from 100 m or so to tens of kilometers, and various attempts have been made to classify them [*Maggs and Davis*, 1968; *Borovsky*, 1993; *Knudsen et al.*, 2001] in terms of their underlying physical properties. In this article, we consider auroral arcs produced by narrow-band field-line resonances (FLRs), with frequencies in the range of a few mHz. The equatorial plasma density and the

0148-0227/05/2004JA010919

length of the resonant field line on which FLRs form largely determine this frequency range. The associated transverse length scales at the ionosphere range from a few kilometers to several tens of kilometers, depending on ambient plasma properties and gradients across geomagnetic field lines. It is now well established [*Thompson and Lysak*, 1996; *Kletzing and Hu*, 2001; *Streltsov et al.*, 2002; *Chaston et al.*, 2003] that small-scale SAWs are a viable candidate for explaining small-scale parallel electric fields measured by low-altitude (up to 1 or 2 Earth radii) Earth-orbiting satellites, such as the recent NASA Fast Auroral Snapshot (FAST) satellite mission [*Carlson et al.*, 1998]. Large-amplitude SAWs with significant field-aligned wave Poynting flux have also been observed by the NASA Polar satellite [*Keiling et al.*, 2001, 2002], and it is interesting to note that transverse scale lengths in satellite observations project (along the magnetic field) into the ionosphere to scales of kilometers, which coincides with the scale length of discrete arcs observed from the ground.

[4] Temporal modulations observed in auroral arcs from meridian scanning photometer (MSP) arrays, as well as the accompanying pulsations in the perturbed magnetic field measured with magnetometers, relate to the time dependence of fundamental resonant standing waves along geomagnetic field lines. In the studies presented by *Samson et al.* [1991, 1992, 2003], discrete arcs, modulated by SAWs at frequencies in the range of a few mHz, were observed. This range of frequencies is associated with standing waves on closed magnetic field lines threading the high-latitude magnetosphere and auroral oval. There are a variety of possible energy sources for these standing SAWs, ranging from MHD surface waves excited by Kelvin-Helmholtz instabilities on boundary layers in the magnetosphere [*Farrugia et al.*, 2000] to MHD waveguide modes [*Samson et al.*, 1992] or magnetospheric cavity modes [*Liu et al.*, 1994]. All of the associated energy sources involve mode conversion of compressional wave energy onto field lines where the compressional wave frequency matches the local field-line eigenfrequency [*Glassmeier*, 1995].

[5] In this article, we shall model the excitation of FLRs observed by ground-based instruments over northern Canada. One of the goals is to explain the observed frequencies of fundamental mode FLRs by taking account of realistic magnetic field geometry [*Cummings et al.*, 1969; *Singer et al.*, 1981; *Rankin et al.*, 2000]. We will also estimate the saturation width of some observed FLRs at the ionosphere by accounting for the integrated effect of wave dispersion on geomagnetic field lines and ionospheric feedback (conductivity enhancements) at the ionosphere. These estimates also allow us to calculate expected phase mixing times [*Mann et al.*, 1995] for FLRs to reach the limiting scale set by gradients in the ambient plasma properties across geomagnetic field lines. Studies such as these are important for interpreting observations of discrete arcs and in determining the controlling factors that influence when and under what circumstances discrete arcs can form. Measurements of quasi-periodic temporal variations of auroral arcs also provide a useful proxy for determining the state of the magnetosphere at a given time along a given set of field lines. This has applications in space weather in what is now termed magnetoseismology [e.g., *Waters et al.*, 1996]. Specifically, by using a realistic geomagnetic field model (eventually global MHD numerical models constrained by solar wind conditions) along with ground-based observations of ULF waves, it may eventually become possible to monitor the global state of the magnetosphere. This will improve forecasting models for space weather.

[6] Below, we analyze three events in which auroral arcs were observed with ground-based MSP, all-sky cameras, and magnetometers. From time series analysis of the observations, we obtain the frequency of the resonant SAW eigenmode. This, in turn, is used to infer the equatorial plasma density along magnetic field lines that connect to the observed discrete arcs. In this analysis, the state of the magnetic field is computed as a function of solar wind parameters from the Tsyganenko 1996 statistical geomagnetic field model [*Tsyganenko and Stern*, 1996]. This is then used as input to a one-dimensional (1-D) linear model of SAWs, in which the density near the equatorial plane is used as a parameter that is fitted to the observed frequency. The density thus obtained is used in a 2-D finite element model of resonant SAWs to study the dispersive saturation properties of the waves [*Lu et al.*, 2003; *Rankin et al.*, 2004]. The outline of the article is as follows. Section 2 gives a brief description of the three events that form the basis of the modeling that is presented. In section 3, we describe a 1-D (along the field line) model of resonant SAWs that can be used to compute standing wave eigenmode frequencies in a general geometry that need not be axisymmetric. This model is used to infer the plasma density in the equatorial plane that connects with the latitudes and longitudes where arcs have been observed. Section 4 presents an analysis of transverse widths and timescales associated with dispersive SAWs in a geometry that is axisymmetric for simplicity, but otherwise the same as that presented in section 3. Section 5 presents results from a nonlinear reduced MHD model of dispersive SAWs. This includes an analysis of the effects of finite ionospheric conductivity, and its modification by the system of currents associated with standing SAWs. Finally, section 6 contains a summary of our results and some concluding remarks.

2. Observations

[7] In this study, we consider three observations of field-line resonances that were made using magnetometer and meridian scanning photometer (MSP) data from ground-based instruments of the CANOPUS array [*Rostoker et al.*, 1995], and the All-Sky Imager (ASI) from the NORSTAR optical imaging array operated by the University of Calgary. The three events correspond to 31 January 1997, 0426 UT; 29 October 1998, 0830–0950 UT; and 9 December 2001, 0100 UT. As a set, the observations cover a substantial portion of the nightside magnetosphere during which ULF (ultra-low-frequency) FLRs were present. In each case, small-scale arcs were seen in the all-sky camera data images, which showed poleward propagating periodically reforming east-west aligned arcs, whose phase propagation is consistent with a FLR. Two of the events, January 1997 and December 2001, were associated with substantial wave power at a frequency around 1.3–1.4 mHz. Both of these observations have been discussed previously in the published literature, the first in the work of *Samson et al.* [2003] and *Lotko et al.* [1998] and the second in the work of

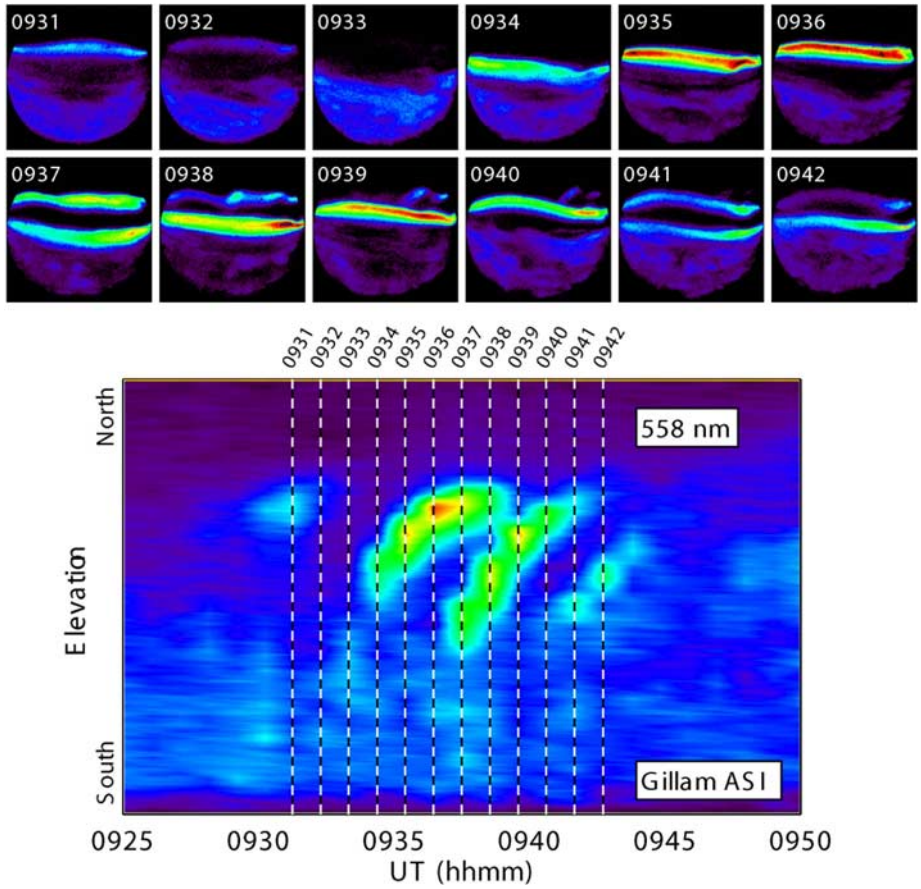

Figure 1. (top) A sequence of auroral images from the all-sky camera at Gillam, Manitoba, on 29 October 1998. The images show a periodically reforming arc that is characteristic of a field-line resonance with a frequency around 5 mHz. The interpretation of this observation is discussed in the text.

Rankin et al. [2004]. The third event, 29 October 1998, shows evidence of wave power at a significantly higher frequency than the other two, 3.8–5.2 mHz, and it is this observation that we focus our attention on in this section of the paper.

[8] Figure 1 shows a sequence of images from the Gillam ASI on 29 October 1998, along with a keogram that indicates poleward propagating periodic wave forms extracted from the ASI measurements from 0925 to 0950 UT. The dashed lines denote the times of the images in the upper part of the figure. Figure 2 shows, in descending order, Gillam MSP data interpolated via the method outlined by *Rae et al.* [2004], and H-component magnetograms from the Churchill line of the CANOPUS magnetometer array. The magnetograms are in descending latitude for 0800–1000 UT on 29 October 1998. The data have been detrended using a running mean of 500 s and band-pass filtered between 1 and 10 mHz. Both the MSP and magnetometer data show two intervals of clear FLR activity. The first interval between 0840 UT and 0930 UT and between 54 to 56 degrees geographic latitude shows evidence of a ~3.7 mHz FLR which phase mixes and significantly intensifies by around 0900 UT. It then fades and is followed by another period of FLR activity at slightly higher latitude, 56 degrees, and frequency ~5.2 mHz at around 0930 UT. The magnetometer data show evidence of wave activity throughout most of the interval.

[9] Figure 3 shows a complex demodulation analysis [e.g., *Beamish et al.*, 1979] of the dominant spectral peak of the FLR at 0855 UT. The data were first high-pass filtered at 1000 s to remove any long-term trends. Figure 3a shows the complex demodulation of the dominant spectral peak at 3.7 mHz. The amplitude of the FLR peaks at around 55 degrees geographic latitude at Gillam. The analysis of this FLR reveals that the H-component amplitude dominates over the D-component, suggesting that the wave is dominantly a toroidal mode FLR. Figure 3b shows the relative phase of the H-(grey) and D-(black) component magnetograms from the Churchill line magnetometers. From Figure 3b, we can see that the H-component displays the classic FLR characteristic of a ~180 degrees phase change across the amplitude peak (and therefore the resonant latitude). The D-component is phase-wrapped and less clear, most probably due to the low amplitude of the signal. Interestingly, complex demodulation analysis of the later FLR from ~0930 to 0945 UT reveals an equatorward propagation of the magnetic signatures, in contrast to poleward propagation of the optical signatures shown in Figure 1. This FLR has a dominant spectral peak at around ~5.2 mHz. One possible explanation for the different

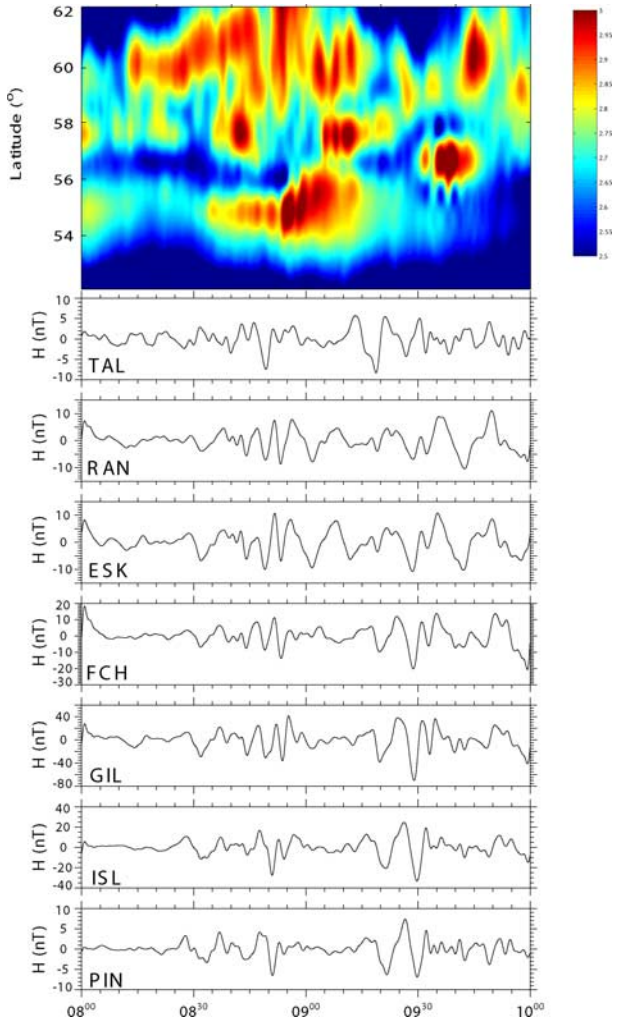

Figure 2. The figure shows meridian scanning photometer and magnetometer data for the arc shown in Figure 1. (top) Data from the Gillam MSP along with the filtered Churchill line (H-component) magnetic field traces. There are two intervals of FLR activity. The first interval is between roughly 0840 UT and 0920 UT, while the second interval is between 0930 UT and 0940 UT at slightly higher geographic latitude.

signature in the magnetometer and optical data is provided by *Allan* [1995], who suggested this might be the result of Biot-Savart integration of ionospheric Hall currents by the magnetometers. In the analysis presented below, we shall analyze this event, along with the other two observations mentioned above.

3. One-Dimensional Eigenmode Analysis of Field-Line Resonances

[10] In this section, we present a 1-D model of standing shear Alfvén waves that incorporates the effects of curvature and magnetic field torsion (twisting). We then apply it to estimate the plasma density profile that would be required along field lines where auroral arcs have been observed. This allows us to determine eigenfrequencies of field lines that match specific observations, as well as providing ambient plasma gradients that control phase mixing on geomagnetic field lines, along with the saturated width of FLRs.

3.1. Shear Alfvén Waves in Model Geomagnetic Fields

[11] In order to compute the frequency and polarization of standing shear Alfvén waves (SAWs) on a given magnetic field line, it is necessary to know the topology of the field line. It can be shown that an orthogonal field-aligned coordinate system does not exist in general for field lines exhibiting curvature and torsion. Thus, it is necessary to introduce a nonorthogonal coordinate system that is similar to that discussed by *Cheng and Zaharia* [2003] and

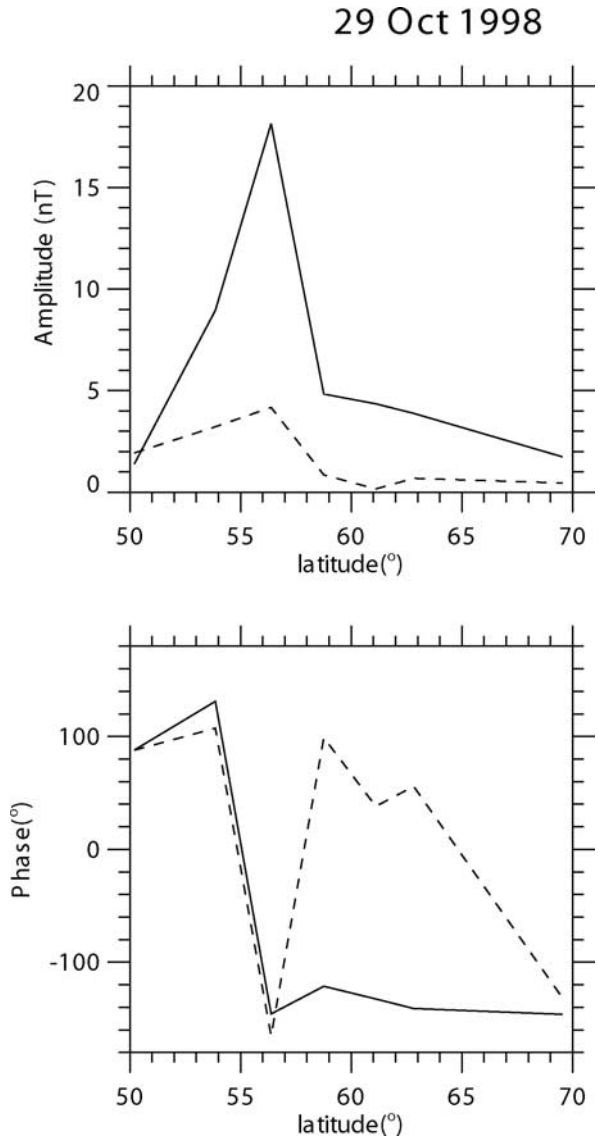

Figure 3. The figure shows complex demodulation of the H- and D-components of the magnetic field for the FLR between 0840 and 0920 UT in Figure 2. The top and bottom parts show the amplitude and phase of the ~3.7 mHz peak, respectively. They are plotted as a function of geographic latitude at 0855 UT. The solid line is for the H-component. The dashed line is for the D-component.

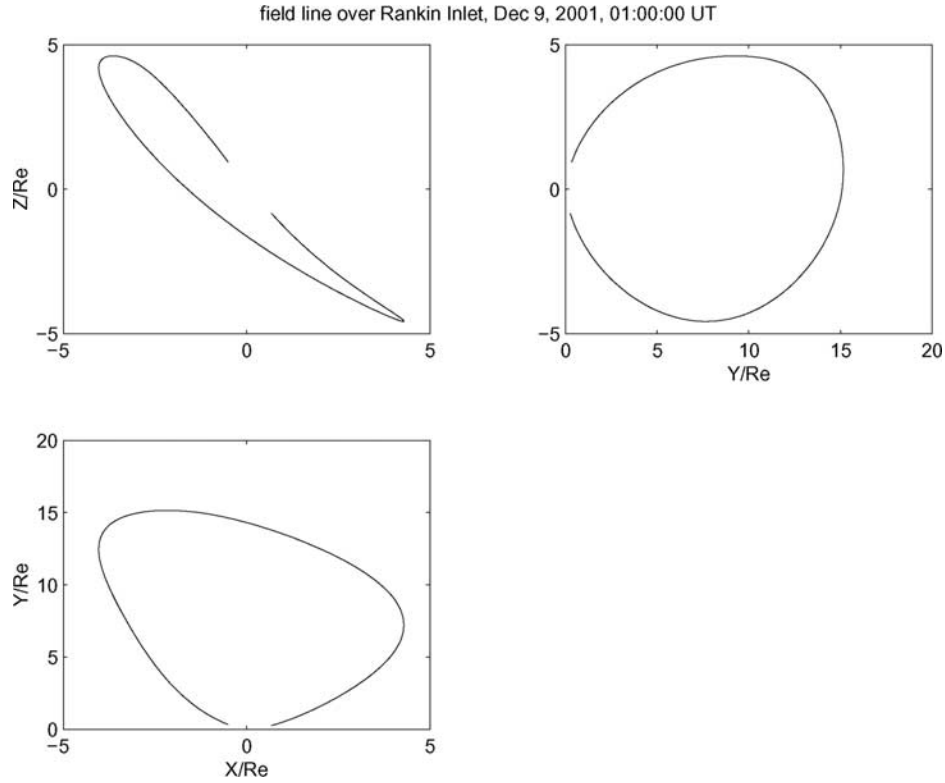

Figure 4. Geomagnetic field lines projected onto the GSM coordinate planes for 9 December 2001, 0100:00 UT. Solar wind conditions correspond to $Dst = -16$, $B_y = -3$ nT, $B_z = +2$ nT, $n = 2.5$ cm^{-3}, and $U_{sw} = 390$ km/s. The solar wind dynamic pressure corresponds to $P = 0.6$ nPa and the dipole tilt is -28.58 degrees.

Proehl et al. [2002]. A full description of the methodology that is required to apply this approach to SAWs in a cold plasma, can be found in the work of R. Rankin et al. (Alfvénic field-line resonances in arbitrary magnetic field topology, submitted to *Advances in Space Research*, 2005). To first order, it can be shown that thermal effects do not significantly change the frequency of long-period (hundreds of seconds) FLRs, and therefore a reasonable approximation is to use the ideal cold MHD equations to estimate frequencies, polarization electric fields, and wave magnetic fields. Then, dispersive properties of the waves can be accounted for as a perturbation on the ideal MHD wave fields. We shall adopt this approach, and first of all solve for the eigenmodes of standing SAWs using geomagnetic field lines specified by the Tsyganenko 96 model, under prescribed solar wind conditions. Our results are more general than those presented by *Rankin et al.* [2000], since we account here for a field-line topology that need not be axisymmetric. The linearized cold ideal MHD wave equations upon which our analysis is based, may be written as

$$\mu_0 \rho \frac{\partial \boldsymbol{V}}{\partial t} = (\nabla \times \boldsymbol{B_0}) \times \boldsymbol{B} + (\nabla \times \boldsymbol{B}) \times \boldsymbol{B_0}$$

$$\frac{\partial \boldsymbol{B}}{\partial t} = -\nabla \times \boldsymbol{E}$$

Here, $\boldsymbol{B_0}$ is the prescribed background field, $\boldsymbol{B}$ is the wave magnetic field variation, $\boldsymbol{V}$ is the perturbation of the plasma fluid velocity, and $\boldsymbol{E} = -\boldsymbol{V} \times \boldsymbol{B_0}$. To proceed, we assume a harmonic time dependence with $\boldsymbol{B} \propto \exp(i\omega\, t)$ and $\boldsymbol{E} \propto i \exp(i\omega\, t)$, respectively. Using the appropriate curl and gradient operators defined by *D'haeseleer et al.* [1991], the covariant-contravariant form of the above equations may be written as

$$\begin{aligned}
\frac{1}{\sqrt{g}} \frac{\partial B_2}{\partial u^3} &= \frac{1}{v_A^2} \left(g^{11} \omega E_1 + g^{12} \omega E_2 \right) \\
\frac{1}{\sqrt{g}} \frac{\partial B_1}{\partial u^3} &= -\frac{1}{v_A^2} \left(g^{12} \omega E_1 + g^{22} \omega E_2 \right) \\
\frac{1}{\sqrt{g}} \frac{\partial E_1}{\partial u^3} &= -\left(g^{12} \omega B_1 + g^{22} \omega B_2 \right) \\
\frac{1}{\sqrt{g}} \frac{\partial E_2}{\partial u^3} &= g^{11} \omega B_1 + g^{12} \omega B_2,
\end{aligned} \tag{1}$$

where g is the determinant of the metric tensor and $v_A^2 = g_{33}(B^3)^2/(\mu_0 \rho)$ describes the variation of the Alfvén speed. The magnetic field is defined by $\boldsymbol{B_0} = \boldsymbol{e_3} B^3$, where $\boldsymbol{e_3}$ is the tangent basis vector in the direction of the ambient field. In this notation, the geomagnetic field is described by $|\boldsymbol{B}_0| = \sqrt{g_{33}} B^3$, where B^3 is the contravariant component in the nonorthogonal field-aligned system of coordinates (u^1, u^2, u^3). Note that in an axisymmetric topology, $g^{12} = 0$, and the field components in equation (1) separate into uncoupled toroidal and poloidal wave modes. In a more general geometry, these modes are coupled, and the metric tensor in equation (1) must be computed numerically. To accomplish this, it is convenient to write the ambient

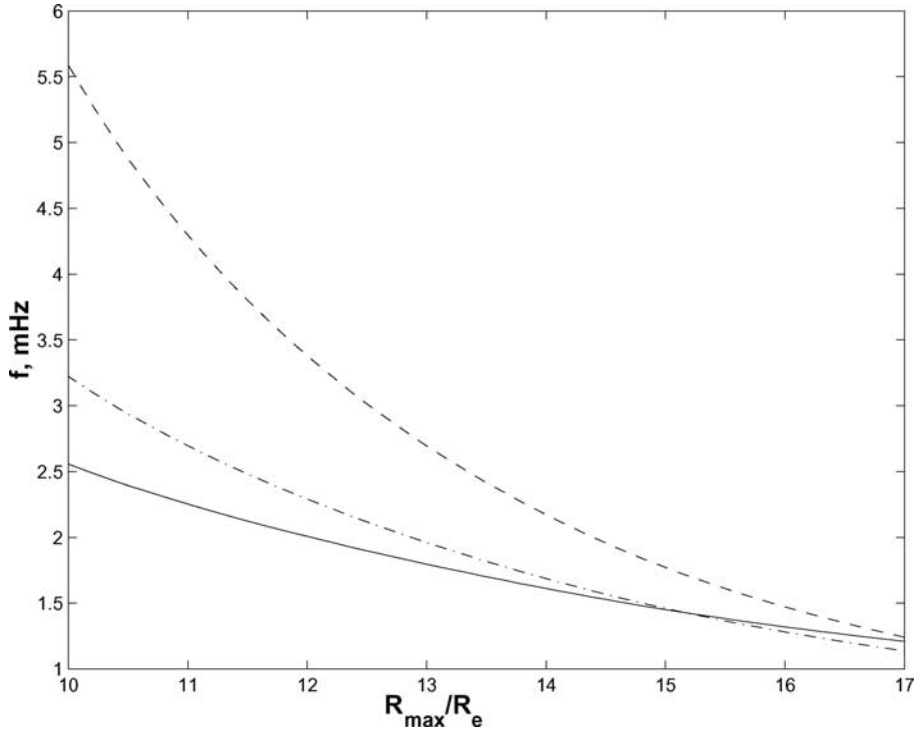

Figure 5. The toroidal mode eigenfrequency plotted as a function of the maximum radial extension (measured from Earth's center) for 9 December 2001. In order to fit the measured frequency of 1.4 mHz, an equatorial plasma has been assumed, along with the variation of density along the field line. The dash-dotted line at the ionosphere corresponds to the density profile used by *Chaston et al.* [2005]. The dashed line is a simple 1/r variation based only on hydrogen. The solid line corresponds to a $1/r^4$ density variation of H along the field line.

magnetic field in terms of Euler potentials defined by $\boldsymbol{B_0} = \nabla\alpha \times \nabla\beta$. By definition, α and β are constant along a given field line. Therefore given a magnetic field model, field lines can be traced from some arbitrary position in the magnetosphere to the northern or southern ionosphere where the Euler potentials can be evaluated. These values are then used for the whole field line, including the original field point in the magnetosphere. The system of equations (1) is solved for each field line that has been traced, using a standard shooting method in which the wave frequency ω and polarization at the ionosphere are determined. The boundary conditions on the electric field at the ionosphere may include finite ionospheric conductivity, but as this changes the eigenfrequency by a small amount [*Allan and Knox*, 1979], we present results for perfect conductivity, in which case the electric field at the ionosphere vanishes.

3.2. Eigenfrequencies for Specific Observations

[12] Using the approach described in section 3.1, we now compute field-line eigenfrequencies for some specific observations. The first case considered corresponds to 9 December 2001 (day of year 343), 0100 UT. For this time, $Dst = -16$, (a quiet day) and the solar wind conditions from ACE correspond to $B_y = -3$ nT, $B_z = +2$ nT, $n = 2.5$ cm^{-3}, and $U_{sw} = 390$ km/s. The solar wind dynamic pressure is $P = 0.6$ nPa and the dipole tilt of Earth is -28.58 degrees. Figure 4 shows three projections of the magnetic field line above the observation point at Rankin Inlet. The geodetic latitude and longitude correspond to 62.82°N and 267.32°E, respectively. Even though the solar wind parameters correspond to "quiet" magnetospheric conditions, this high-latitude field line is not particularly dipolar. It has a length of 40.7 R_E, a maximum radial extension (measured from the center of the Earth) that corresponds to 15.39 R_E, and a minimum magnetic field strength of 17 nT along the field line. Figure 5 shows the toroidal mode eigenfrequency as a function of radius (maximum field-line radial extension from Earth) for this observation. In order to fit the measured frequency of 1.4 mHz, an equatorial plasma density has been specified, along with the variation of density along the field line. We initially choose the density profiles specified in Table 1 of *Chaston et al.* [2005], which are based on satellite measurements of an $L = 14$ field line at 0900 MLT (we shall see that the precise form of the density profile along the field line is not particularly important in fitting the frequency).

[13] To illustrate the effect of field-line topology on standing SAW eigenmodes, we first of all solve for the wave frequency and polarization in an axisymmetric situation. In order to match the frequency of the 9 December 2001 observation, we used an equatorial density of 0.38 amu/cm^3 that consists of a mixture of 0.36 amu/cm^3 hydrogen (with field-aligned variation $1/r^3$) and 0.02 amu/cm^3 oxygen (with a field-aligned variation $1/r^2$). This is indicated by the dash-dotted line in Figure 5, which shows the computed frequency versus maximum radial extension

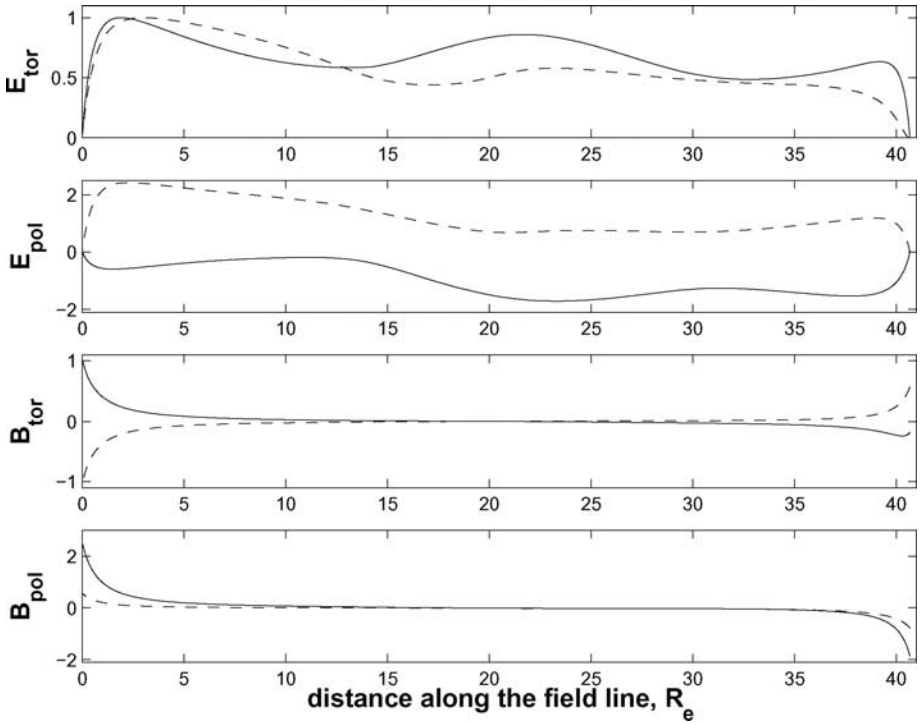

Figure 6. The figure shows model results corresponding to the FLR observation reported on 9 December 2001. The electric and magnetic fields along the field line are sketched for two fundamental wave modes having polarizations at the northern ionosphere of 86° and 82°, respectively. The periods of the wave modes are 1000.22 s (solid lines) and 492.39 s (dashed lines), respectively. The wave fields have been projected onto the toroidal (azimuthal) and poloidal directions. Solid lines correspond to the mode with a period of 1000.22 s, while dashed lines correspond to the mode with a period.

of the field line. The oxygen contribution turns out to be relatively unimportant in affecting the eigenfrequency and is neglected in the remainder of this paper. For comparison, the dashed line in Figure 5 corresponds to a 1/r variation of the density of H^+ along the field line, while the solid line assumes $1/r^4$. Figure 5 demonstrates that the density variation along the field line does not have a strong effect on the frequency of high-latitude FLRs for field lines poleward of the observation. Upon using the nonaxisymmetric covariant analysis (with the same density profile), we find that there are two fundamental wave modes having roughly the same polarization at the ionosphere (86° and 82°, respectively, where 0° corresponds to east-west alignment and 90° corresponds to north-south). The periods of these two modes are 1000.22 s and 492.39 s, respectively. In spite of the large difference in their periods, both polarizations correspond to fundamental modes, since their electric fields have nodes only at each ionosphere. In a dipole field, a polarization of 90° at the ionosphere corresponds to a poloidal mode SAW, and therefore it is tempting to identify the larger-period wave as the poloidal-like mode. However, this designation is approximate at best, as the polarization of each mode computed from our analysis changes significantly along the field line. This is illustrated in Figure 6, where the **E** and **B** fields of the computed eigenmodes have been projected onto the corresponding toroidal and poloidal directions. The solid lines correspond to the mode with a period of 1000.22 s, while dashed lines correspond to the mode with a period of 492 s. In the case of the mode with the larger period, the observed frequency of 1.4 mHz is fitted, using a factor of two smaller equatorial density than in the axisymmetric case. We note that in the published literature, the claim has been made that magnetospheric FLR frequencies are anomalously low, requiring abnormally high magnetospheric plasma densities. The model results for this particular observation suggest otherwise, and in particular, the required equatorial plasma densities are, if anything, quite low.

[14] We turn now to a consideration of the event of 31 January 1997, 0426:00 UT. For this day, $Dst = -15$ and the solar wind conditions correspond to $B_y = -3$ nT, $B_z = -1$ nT, $n = 3.5$ cm^{-3}, and $U_{sw} = 600$ km/s. The solar wind dynamic pressure was $P = 2.0$ nPa. These data are from IMP 8, which was in the solar wind on the flank of the magnetosphere. The dipole tilt for this day was 27.86°. Figure 7 shows the three GSM projections of the T96 field line over Gillam, which is located at geodetic latitude and longitude of 56.38° and 265.36°, respectively. The length of the field line projected above the observation point is 24.6 R_E. The maximum radial extension of the field line is 10.97 R_E, and the minimum geomagnetic field strength along the field line is 18.98 nT. In this case, an equatorial plasma density of 5.43 cm^{-3} is necessary to explain the observed frequency of 1.3 mHz. The dashed line in Figure 8 corresponds to a 1/r variation of H along the T96 field line, while the solid line assumes $1/r^4$. Again, the dependence of the frequency on the density variation along the field line is not particularly strong on field lines

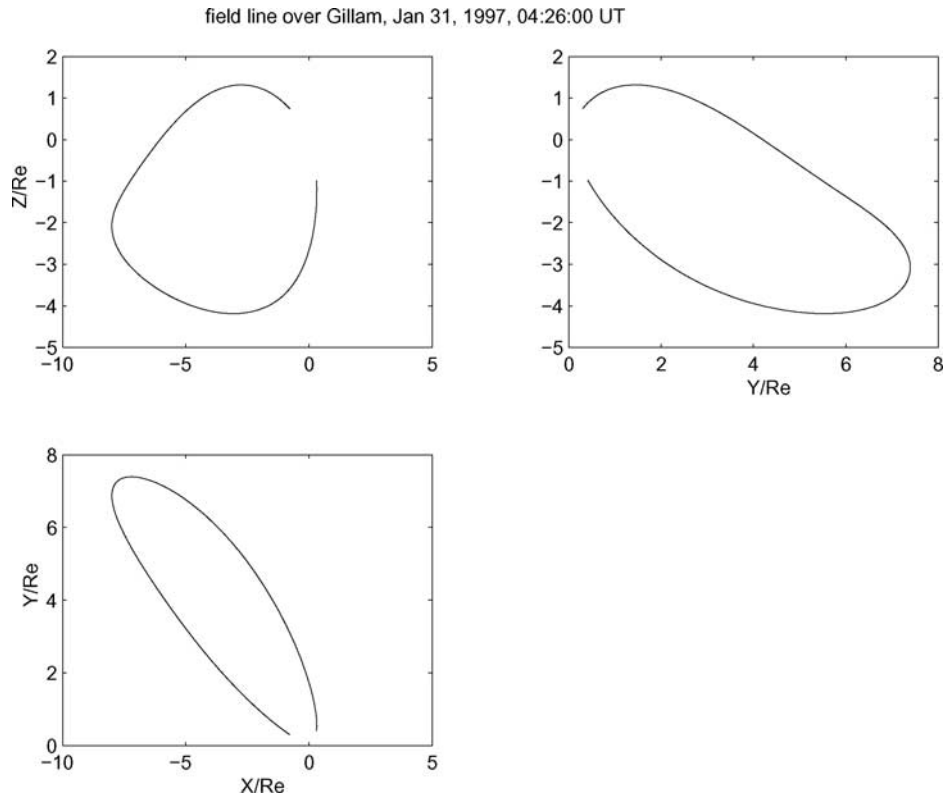

Figure 7. Geomagnetic field-line projections for 31 January 1997, 0426:00 UT. For this day, $Dst = -15$ and the solar wind conditions correspond to $B_y = -3$ nT, $B_z = -1$ nT, $n = 3.5$ cm^{-3}, and $U_{sw} = 600$ km/s. The solar wind dynamic pressure was $P = 2.0$ nPa. The dipole tilt for this day was 27.86 degrees.

poleward of the observation point. The somewhat high plasma sheet density that is required to fit this observation is suggestive of terminology that has been used to describe nightside FLRs, i.e., ''anomalously low.'' Within the uncertainties of the approximate FLR and magnetic field models that have been used, it is rather difficult to reach a general conclusion. It may simply be that a better field-line model is required in this particular case.

[15] The third and final FLR observation is that pertaining to 29 October 1998 between roughly 0840 UT and 0940 UT. The solar wind conditions correspond to $Dst = -4$, $B_y = -3$ nT, $B_z = +5$ nT, $n = 6$ cm^{-3}, and $U_{\rm sw} = 600$ km/s. The solar wind dynamic pressure was $P = 3.6$ nPa. Figure 9 shows the field-line projections for this observation at the location of Gillam. In this case, the measured frequency of $\sim$5.2 mHz at 0940 UT is fitted using an equatorial plasma density of 0.9 amu/cm^3 at $L = 10$ (with 1/r variation along the field line). Using this density profile, the frequency supported by the field line directly above the observation point is followed through the evolving magnetic topology until 0840 UT, where it reaches $\sim$3.8 mHz. This is shown in Figure 10, along with the variation in the FLR wave dispersion parameter that will be discussed below. The frequency variation predicted by the eigenmode analysis presented in section 3.1 is very close to what is measured and is perhaps suggestive of wave power being fed to field lines at a range of frequencies, rather than a single (monochromatic) frequency. Alternatively, the magnetospheric waveguide or cavity mode that possibly feeds this FLR may be changing frequency due to the effect of the solar wind. In section 4, we discuss another possibility related to the effect of gradients in wave dispersion perpendicular to geomagnetic field lines.

4. Characteristic Space and Timescale Estimates

[16] The frequency characteristics of geomagnetic field lines have been considered in section 3.2 for three ground-based observations of FLRs. We now consider characteristic space and timescales for wave dispersion, in order to provide a more complete interpretation of the observations. Wave dispersion becomes particularly important at perpendicular length scales comparable to the electron inertial length (skin depth) or the ion acoustic gyroradius. The former is important in standing SAWs near the ionosphere, while the latter is related to the plasma sheet temperature in the vicinity of the equatorial plane. As a preamble, we will note that FLRs involve oscillations of an entire field line, and just as the frequency is a characteristic of the entire field line, so too is wave dispersion. In the discussion and analysis that follows, we summarize the results from a simple model of dispersive FLRS and show how wave dispersion is related to the saturation width and formation time of FLRs. Our analysis is thus far limited to axisymmetric field topologies, and therefore it provides only an approximation of the dispersion that may be present in the observations discussed above.

[17] Following the analysis presented by *Rankin et al.* [1999a] and restricting our analysis to linear waves with

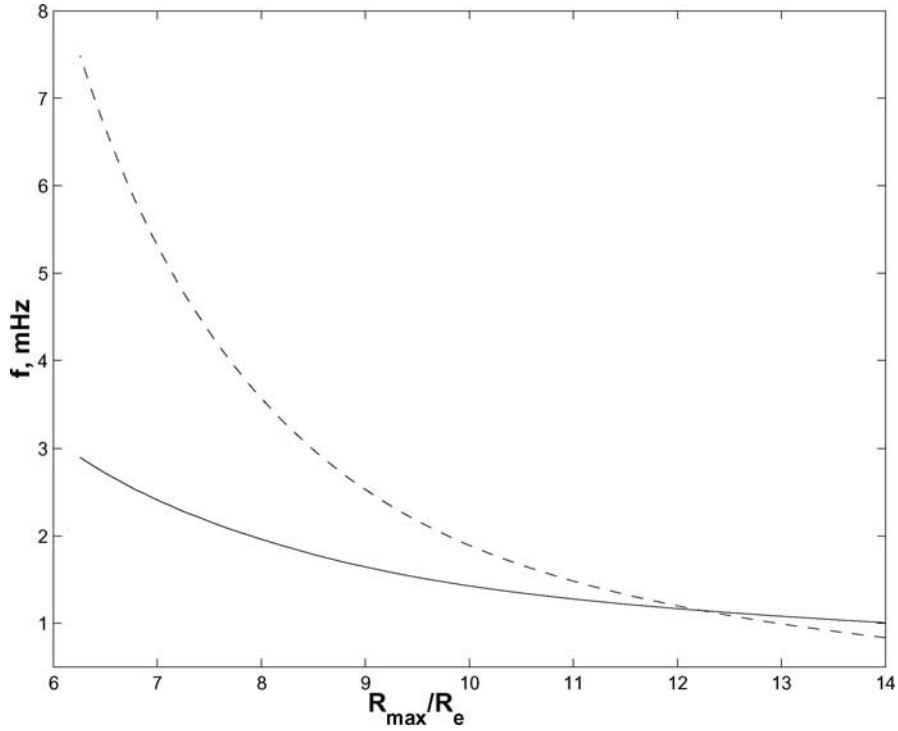

Figure 8. The toroidal mode eigenfrequency plotted as a function of maximum radial extension of the field line for 31 January 1997. The solid line is a simple 1/r variation based only on hydrogen. The dashed line corresponds to a $1/r^4$ density variation along the field line. The Tsyganenko 1996 geomagnetic field model is used.

small azimuthal wave number in an axisymmetric magnetosphere, we first of all write the SAW azimuthal magnetic field component as $h_2 B_\phi = h_2^{eq} B_0^{eq} b(x, t) B_1(l) \exp i(m\phi - \omega_0 t)$, where $h_2 = \sqrt{g_{22}}$ is the metric coefficient in coordinates associated with the geomagnetic field, B_0^{eq} is the ambient magnetic field strength at the equator, $B_1(l)$ is the SAW eigenfunction along the field line (defined using equation (1) in the axisymmetric situation), and $b(x, t)$ is the SAW slowly varying amplitude. The latter grows with time in response to an external driver which represents compressional waves trapped inside the magnetospheric cavity. The coordinate l is measured along geomagnetic field lines with respect to the equator, and x is the earthward directed perpendicular coordinate relative to a given magnetic field line at the equator. Referring again to *Rankin et al.* [1999a], it is possible to write the evolution equation for $b(x, t)$ as

$$\frac{\partial b}{\partial t} - i\omega_0 \frac{\partial}{\partial x}\left(\delta \frac{\partial b}{\partial x}\right) = i(\delta\Omega - \Delta\omega) b + \omega_0 R$$
$$\delta\Omega = \frac{1}{2\omega_0 L^2 R_e^2} \int dl v_A^2 \frac{h_1}{h_2} \frac{\delta\rho}{\rho} \left(\frac{\partial B_1}{\partial l}\right) \tag{2}$$

Here, $\Delta\omega(x) = \omega_{SAW} - \omega_0$ is the ideal MHD eigenfrequency detuning across magnetic shells, $R(x,t)$ is the amplitude of the model SAW driver, $h_1 = \sqrt{g_{11}}$ is the metric coefficient associated with the direction perpendicular to magnetic flux surfaces, and $\delta\Omega$ is a nonlinear frequency shift related to the amplitude of density perturbations ($\delta\rho/\rho$) excited on geomagnetic field lines by SAW ponderomotive forces. We consider the nonlinear frequency shift as a free parameter in order to illustrate how steepening of the perpendicular density profile affects phase mixing to the scale at which dispersive effects become important. In equation (2), the field-line dispersion parameter $\delta(x)$ is defined by

$$\delta = L^2 R_e^2 \int dl \left(\frac{3}{4} \frac{\rho_s^2}{\omega_0^2} \frac{V_A^2}{h_3} (\partial_l B_1)^2 + \frac{V_{Te}^2}{\omega_0^2 h_3} (\partial_l B_1) \partial_l \left(B_1 \lambda_e^2\right) - \frac{\lambda_e^2}{h_3} B_1^2 \right) \tag{3}$$

where ρ_s is the ion acoustic gyroradius, λ_e is the electron skin depth (inertial scale), V_{Te} is the electron thermal speed, $h_3 = \sqrt{g_{33}}$ is the geomagnetic field-aligned metric coefficient, and the integral is taken over the total length of the magnetic field line. Equation (2) describes phase mixing on the gradient in the Alfvén speed across geomagnetic field lines. It is affected by the dispersion parameter, $\delta(x)$, that has three contributions corresponding to finite ion acoustic gyroradius, electron temperature, and electron inertia, respectively. The two thermal contributions provide positive dispersion, while electron inertia gives a contribution that is negative. This designation for δ refers to the sign of the group velocity, when computed from $\omega(x) \sim \Delta\omega(x) + \omega_0(1 + k_\perp^2 \delta)$, which is valid in the WKB approximation. Although the ambient density and temperature can change by orders of magnitude along a field line, low-frequency FLRs satisfy $k_\perp^2 \delta \ll 1$ throughout most of the magnetosphere. Therefore dispersive effects in standing SAWs can be regarded as a small perturbation on the ideal MHD eigenmodes discussed earlier in the paper.

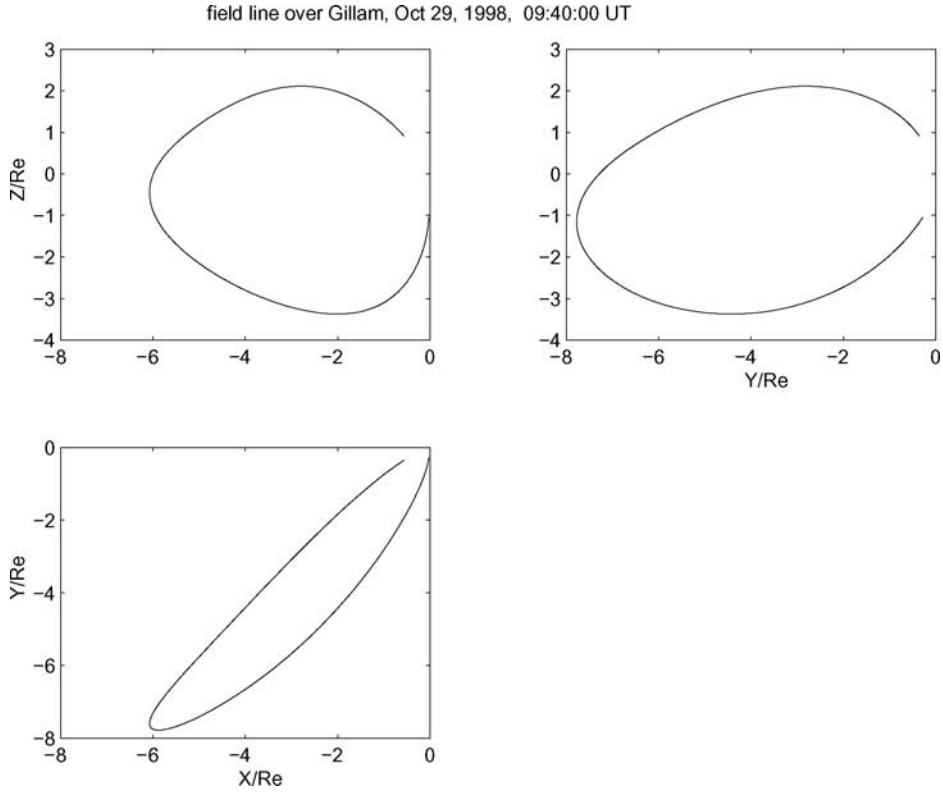

Figure 9. Geomagnetic field-line projections for 29 October 1998, 0940 UT. The solar wind conditions correspond to $Dst = -4$, $B_y = -3$ nT, $B_z = +5$ nT, $n = 6$ cm^{-3}, and $U_{sw} = 600$ km/s. The solar wind dynamic pressure was $P = 3.6$ nPa.

[18] Comparing respective dispersion and linear eigenfrequency detuning terms in equation (2) allows us to determine the characteristic time of formation of FLRs, along with the associated transverse spatial scale that represents a balance between inward (perpendicular) Poynting flux and dispersive wave propagation out of the resonance at small spatial scales. In this situation, we obtain

$$\omega_0 t_{dis} = 2\left(l_\omega^2/\delta\right)^{1/3}, \quad l_{dis} = (\delta l_\omega)^{1/3}, \quad b_{dis} = R\left(l_\omega^2/\delta\right)^{1/3} \qquad (4)$$

where quantities from left to right are the linear dispersive saturation time, width, and amplitude, respectively, while l_ω is the length scale of the gradient in the Alfvén speed. In the situation where nonlinear frequency detuning (by wave ponderomotive forces) or transverse gradients in wave dispersion are important, there are two additional characteristic timescales defined by

$$\omega_0 t_{NL} = \frac{l_\omega}{\sqrt{\delta}} \Big/ \sqrt{\left(\frac{\delta\Omega}{\omega_0}\right)}, \quad \omega_0 t_c = 1/\sqrt{|\beta|/l_\omega} \qquad (5)$$

Their associated spatial scales are comparable to the linear dispersive saturation width in equation (4). Note that the first (nonlinear) timescale defined by equation (5) involves an intermixing of wave ponderomotive and dispersive effects. The second timescale in equation (5) is related to earthward defocusing of SAWs by the transverse gradient β in the wave dispersion parameter. This is computed using the dispersion parameter defined above, from the assumption that it can be written as $\delta = \beta x$ in the vicinity of the field line where FLRs are excited. For 29 October 1998, observation discussed above, Figure 10 shows that the dispersion parameter varies strongly over the timescale for

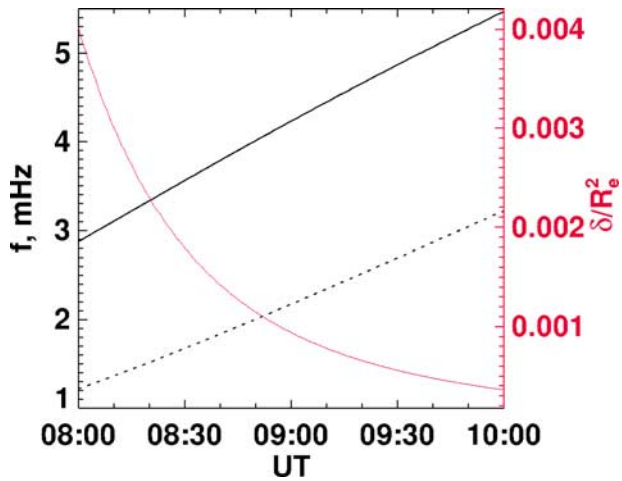

Figure 10. The toroidal mode eigenfrequency plotted as a function of time for 29 October 1998. The frequency supported by the field line directly above the observation point is plotted against time, for comparison against the MSP data shown in Figure 2. The solid line in the frequency plot corresponds to the toroidal mode. The black dashed line shows the poloidal mode. The figure also shows the variation of the dispersion parameter (in red) discussed in the text.

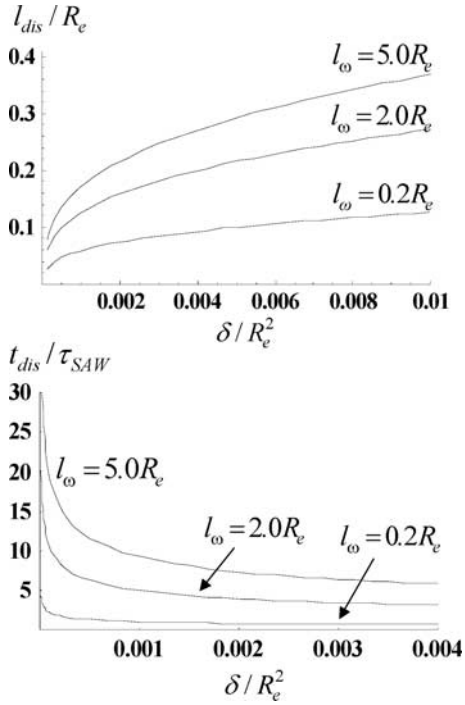

Figure 11. Estimates based on equation (4) of (a) the FLR linear dispersive saturation width and (b) the corresponding saturation time as a function of the wave dispersion parameter. The three curves on each figure correspond to different Alfvén speed gradients perpendicular to the geomagnetic field.

which FLR activity is observed. The associated spatial gradient in dispersion, along with the computed transverse gradient in the Alfven speed profile, corresponds to a defocusing time of around 10 SAW periods (computed using t_c in equation (5)), which is quite comparable to the linear phase mixing time. This perhaps suggests that the variation in FLR frequency from around 3.8 mHz to 5.2 mHz in this observation is associated with a distributed source that feeds wave power to the range of field lines on which the FLR is observed.

[19] We now consider the linear phase mixing and SAW ponderomotive force estimates provided by equations (4)–(5) and discuss them in the context of the FLR observations discussed in section 3.2. Figure 11 shows estimates based on equation (4) of the linear dispersive saturation timescale and the corresponding saturation width as a function of the dispersion parameter. The three curves on each figure correspond to different Alfvén speed gradients perpendicular to the geomagnetic field. As we shall see below, the typical value of the dispersion parameter for the range of field lines covered by the observations is around $\delta \sim 10^{-3}$ R_e^2, in which case the characteristic resonance width in the equatorial plane, taking $l_\omega = 1.0\ R_e$, is around 0.08 R_E, while the phase mixing time is roughly 4 Alfvén periods. For $l_\omega = 5.0\ R_E$, the characteristic equatorial width is around 0.16 R_E, while the phase mixing time rises to around 9 Alfvén periods. The latter estimates are in good agreement with the range covered by the observations, which correspond to $l_\omega = 4.4\ R_e$ for 9 December 2001 and 31 January 1997 events, while the 29 October 1998 event has $l_\omega = 3.7\ R_E$. For comparison, in Figure 12, we plot the nonlinear phase mixing timescale as a function of the dispersion parameter, for $l_\omega/R_e = 0.2$ (1.0) and nonlinear frequency shift $\delta\Omega/\omega_0 = 0.1$ (0.4). This translates into density fluctuations of order 10 (40) percent along geomagnetic field lines where FLRs form. It can be seen that phase mixing through steepening of the Alfvén speed profile also requires a few periods. In this situation, as shown by *Lu et al.* [2003], there is expected to be significant nonlinear structuring of FLR wave fields in latitude owing to a strong interaction of dispersive waves with density fluctuations that act to trap SAWs within them. This effect should enhance parallel electric fields in FLRs due to the increase in $k_\perp$ that arises from steepening of the Alfvén gradient across field lines. This type of effect is encouraging in terms of attempts to explain auroral particle acceleration in FLRs, as observed in the meridian scanning photometer data in Figure 1.

[20] Figure 13 shows the dispersion parameter as a function of maximum radial field-line extent for the three observations presented in section 3. In obtaining these curves, we have assumed plasma sheet electron and ion temperatures of 250 eV and 2 keV, respectively. The density profiles along field lines are based on 1/r (top) and $1/r^4$ (bottom) density variations, with equatorial plasma densities chosen to match the SAW eigenfrequency for each observation. The temperature variation along geomagnetic field lines is based on the assumption of constant plasma pressure. Linear space and timescale estimates discussed above can be computed using these figures, provided the equatorial intersection of each field line is known. Although Figure 13 is specific to the solar wind conditions selected for the present studies, it should be useful in general for estimating characteristic widths and timescales for auroral arc formation under ''fairly typical'' solar wind conditions.

5. Solutions to the Reduced MHD Equations With Dispersion and Ionospheric Damping

[21] Thus far, we have not considered the effects of ionospheric damping on the evolution of dispersive scale FLRs. If the ionospheric conductivity is large, FLRs will narrow to dispersive scales and propagate away from where

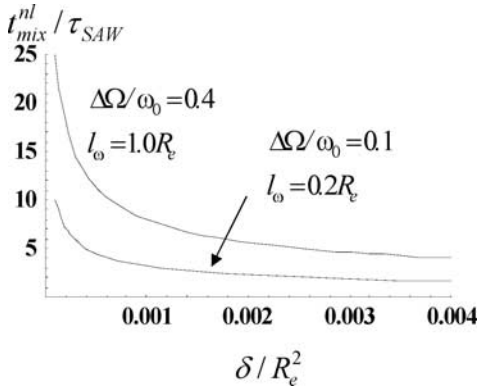

Figure 12. The nonlinear phase mixing timescale as a function of the dispersion parameter, assuming Alfvén speed gradients $l_\omega/R_e = 1.0$, 0.2 and a nonlinear frequency shift corresponding to $\delta\Omega = 0.4\omega_0$, $0.1\omega_0$, respectively.

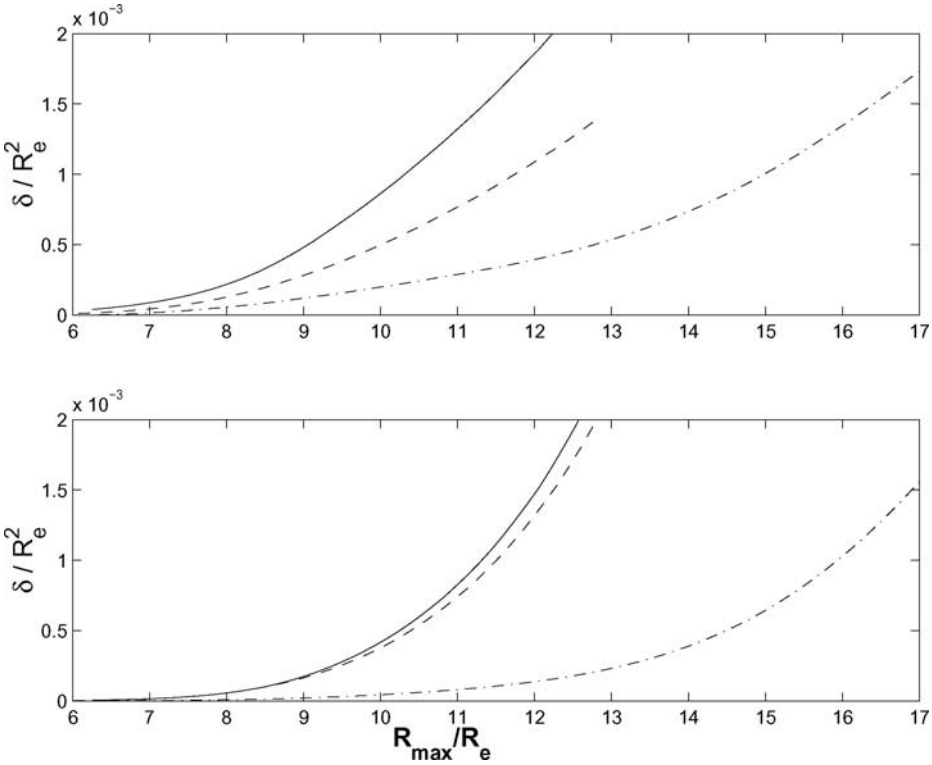

Figure 13. The wave dispersion parameter as a function of radius measured from the geographic equator, for the three observations presented in section 2. Plasma sheet electron and ion temperatures of 250 eV and 2 keV have been assumed. The profiles are based on (top) 1/r and (bottom) $1/r^4$ density variations along the geomagnetic field line, with equatorial plasma densities chosen to match the SAW eigenfrequencies for each observation. The temperature variation along geomagnetic field lines is based on the assumption of constant plasma pressure. Solid line corresponds to 31 January 1997; dashed line corresponds to 29 October 1998; dash-dotted line corresponds to 9 December 2001.

they are excited. This can potentially result in multiple arcs, each of which has a characteristic width $k_{\perp}^{-1}$. Finite ionospheric conductivity will damp FLRs and lead to their localization on geomagnetic field lines where the shear Alfvén wave frequency matches the compressional wave driver frequency. On the other hand, if the ionospheric conductivity is too low (below about 0.5 S), the amplitude of the resulting wave fields may not be large enough to allow the FLR to grow to significant amplitude. A compromise is required; the ambient conductivity must be such that it allows field-aligned currents in SAWs to grow to a level where they can potentially modify the conductivity. We shall demonstrate that this type of feedback effect can result in large-amplitude, localized FLR wave fields that are consistent with observations.

[22] Different mechanisms have been invoked to explain how field-aligned currents in SAWs can lead to a modification of the ionospheric Pedersen conductivity. One such mechanism was investigated by *Prakash et al.* [2003], who demonstrated that FLR dissipation can overcome wave dispersion provided the dispersive saturation width is initially larger than the characteristic ionospheric dissipation scale:

$$l_{diss} \sim \gamma l_{\omega}/\omega_0, \quad \gamma = \frac{1}{\mu_0 \sum_p N}\left[B_1^2(l)\frac{h_1}{h_2}\right]_{l_{\max}} \tag{6}$$

Here, N is a normalization constant for the SAW eigenfunction $B_1(l)$ along the field line, γ is the SAW damping rate, $\sum_p$ is the Pedersen conductance, and the second expression on the right is evaluated at the ionosphere. When the Pedersen conductance is allowed to vary in response to the modulation of electron precipitation by SAWs, it leads to a modification of damping in equation (6). Averaging over a wave cycle leads to the expression

$$\bar{\gamma} = \frac{\gamma_0}{2}\left[1 + \frac{1}{\pi}\int_0^{\pi} \frac{d\alpha}{\left(1 + \sigma_p^2\left|\frac{\partial b}{\partial x}\right| \sin\alpha\right)^{1/2}}\right] \tag{7}$$

Here, $\sigma_p = Q\sum_p(0)(K_e B_0^{Ion} B_1(l_{\max})/e\mu_0)^{1/2}$, where K_e is the energy of precipitating electrons, $Q(K_e)$ is a function of energy defined by, for example, *Robinson et al.* [1987], and γ_0 is the initial SAW damping rate. An immediate problem follows from equation (7). It is clear that irrespective of the precipitation energy, ionospheric losses in FLRs can at most be reduced by a factor of two. This means that in regions of low ambient conductivity, precipitation is not very effective at changing the ionospheric conductivity under FLRs. This limitation in the reduction of damping is missing from 2-D models of FLRs that rely on the modulation of electron precipitation as a mechanism for changing the ionospheric

Pedersen conductivity. Such models do not account for azimuthal phase velocities (and the associated 180° latitudinal phase shift across FLRs), and it is this characteristic which allows conductivities to be enhanced only during the upward half-cycle of field-aligned currents causing precipitation. We shall now demonstrate that nonlinear electron heating of the ionosphere by the wave fields of long-period SAWs can potentially be more effective at modifying regions of initially low ambient conductivity.

[23] In the following, we use a simple model of the ionosphere in which electron cooling takes place through elastic collisions with neutrals. While other collision processes potentially play an important role, we defer for future study the rather complicated chemistry of the ionosphere in order to demonstrate the basic idea behind our proposed nonlinear heating mechanism. Nonlinear electron heating by SAWs can be understood from the electron part of the ionospheric Pedersen conductivity,

$$j_{\perp e} = \sigma_{pe} E_\perp = j_\perp \frac{\nu_e}{\nu_i} \frac{\Omega_i}{\Omega_e}, \tag{8}$$

where $\nu_e \sim 10^4\ s^{-1}$ and $\nu_i \sim 10^2\ s^{-1}$ represent typical values for the electron and ion collision frequencies and $\Omega_{e,i}$ are the respective gyrofrequencies. Taking typical values for the conductivity, $\sigma_{pe} = 5 \times 10^{-7}$ S/m, and electron Pedersen current, $j_{\perp e} = 0.005 j_\perp$, we obtain a heating power $W_{Te} = 0.005 W_{Ti} \sim 10^{-9}$ W/m^3 or roughly 0.2 eV/s. While this heating rate for electrons is much less than for ions, the losses for electrons due to collisions are also much less. Therefore heating of electrons by long-period field-aligned currents in SAWs turns out to be significant, leading to ionization and significant changes in the ambient Pedersen conductance. In the case of long-period SAWs (frequencies on the order of a few mHz), the ionization in the E layer due to electron heating can be represented by the steady state system of equations

$$\begin{aligned} n_e^2 - n_{e0}^2 &= \frac{\nu_{ioniz} n_e}{R}, \\ \frac{j_\perp^2}{\sigma_{p0}} &= \frac{n_e^2}{n_e^0} \nu_i (T_e - T_n) \end{aligned} \tag{9}$$

where $n_e^0 = \sqrt{S/R}$ is the unperturbed electron density, T_e and T_n are the ionospheric electron and neutral temperatures, respectively, S represents an external source of ionization, and R is the corresponding recombination rate. The ionization rate based on the typical ionization potential of molecular oxygen or nitrogen is estimated from $\nu_{Ioniz} \sim 0.1 \nu_e \exp(-I/2T_e)$.

[24] Nonlinear electron heating has been incorporated into a 2-D reduced MHD numerical model that describes the excitation of dispersive shear Alfvén waves in an axisymmetric field topology [*Lu et al.*, 2003]. Although we are not yet able to deal with the more complicated topology associated with the observations described in section 3, our model does take account of field-line stretching, and the variation of ambient parameters that is necessary to describe saturation effects due to wave dispersion and finite ionospheric conductivity. The reader is referred to *Lu et al.* [2003], where the equations solved in the numerical model are described. The ionospheric boundary is placed at an altitude of 100 km, and the finite element model TOPO [*Marchand and Simard*, 1997] is used to solve the two-dimensional SAW MHD equations.

[25] Figure 14 shows the field-aligned current at the ionosphere, using parameters that approximate the 9 December 2001 event. The length of the field line is 35 R_E, while the equatorial density is chosen so as to give a frequency of 1.4 mHz that matches the observation seen from the ground. The top two parts in Figure 14 show the field-aligned and ionospheric current densities as a function of the coordinate perpendicular to the field line. The bottom part shows the Pedersen conductance at the time of saturation, which is around 20 Alfvén periods. The initial ambient Pedersen conductance is 1 S, and it can be seen in the bottom part of Figure 13 that it saturates at around 11.5 S due to electron heating by the system of currents in SAWs. Figure 15 shows the azimuthal magnetic field of the SAW, together with the associated parallel current density and perpendicular electric field strength along the field line at an intermediate position across the resonance (roughly 0.06 R_E). The half-width of the arc (envelope) is roughly 125 km, which is quite comparable to the scale found in the ASI data for this observation [*Rankin et al.*, 2004]. On decreasing the amplitude of the driver for the SAW by fifty percent, we obtain smaller parallel currents that saturate at around 3.5 μA/m^2, with wave magnetic field amplitudes around 60 nT and Pedersen conductance increases of a factor of three over the ambient conductance. In both situations, wave dispersion plays a significant role in determining the spatial scale of the saturated FLR, but structuring of the FLR due to dispersive effects is not very obvious. In the future, we will consider nonlinear effects due to profile steepening by SAW ponderomotive forces. As discussed earlier and verified by *Lu et al.* [2003], this effect is necessary in order to see electron inertial scale arcs within the envelope of FLR wave fields.

[26] With respect to the other two events reported in this paper, we obtain similar results to those shown in Figures 14 and 15. In order to fit each observation, it is necessary to choose an initial ambient conductivity along with the amplitude of the driver that excites SAWs in our model. It is these two effects that determine the spatial scale of the FLR at saturation. In the absence of finite conductivity, one obtains a series of dispersive scale arcs that stand across a sizeable fraction of the inner magnetosphere. Therefore we conclude that the essential ingredients for observing localized dispersive scale arcs are finite ionospheric conductivity and electron heating, which gives rise to conductivity increases within the system of field-aligned current forming the arc. The scale sizes reported for the cases with finite Pedersen conductivity are in agreement with the estimates provided by equation (4). In particular, once heating elevates the Pedersen conductivity to a few Siemens, the ionospheric layer under the FLR becomes highly reflective. The actual scale of the arc obtained from the model can be easily made to fit the observations by varying the initial ambient conductivity from 1 to 2.5 S.

6. Conclusions

[27] In this article, we have discussed three observations that all show evidence of ULF wave activity in the Pc-5

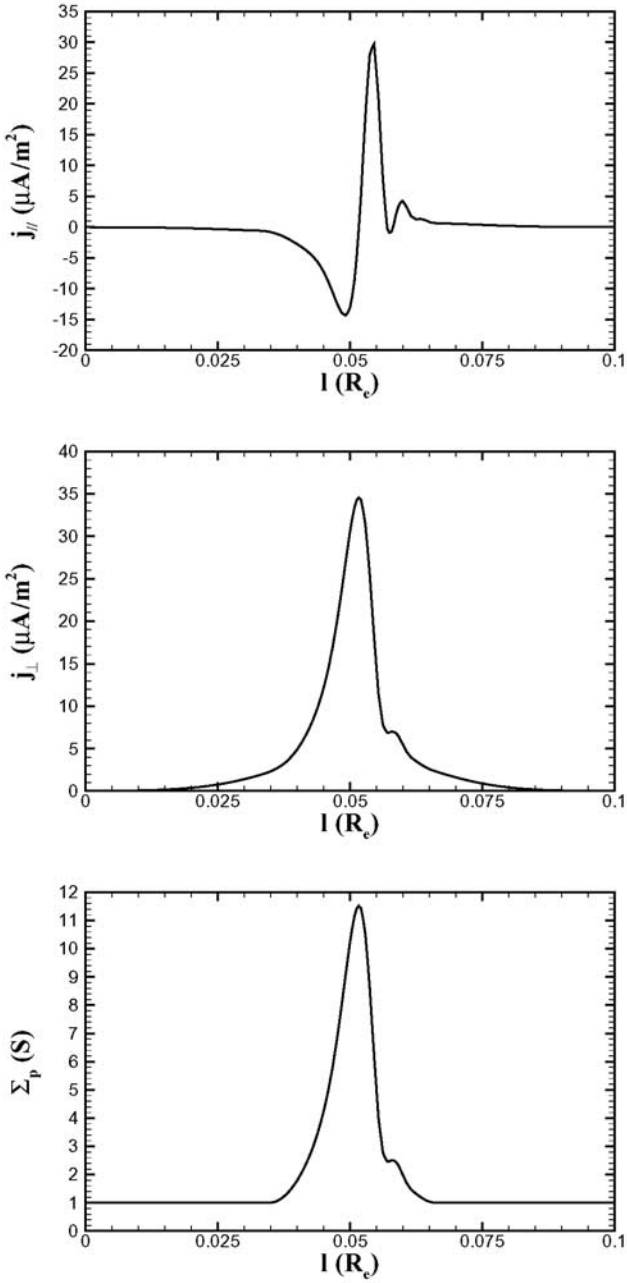

Figure 14. From top to bottom is shown the field-aligned current density, the perpendicular current density, and the Pedersen conductance computed using a two-dimensional reduced MHD dispersive FLR model, with nonlinear electron heating included as an ionospheric boundary condition. The initial Pedersen conductance is 1 S. Results are shown at the ionsopheric end of the field line at a time corresponding to 20 SAW periods. The field line has ambient parameters appropriate to the 9 December 2001 observation discussed in the test.

range of geomagnetic pulsations. In each case, discrete mode field-line resonances (FLRs) are observed, with clear signatures seen in all-sky camera data and in meridian scanning photometer and magnetometer data. Two of the FLR-related arcs are associated with near monochromatic wave energy centered on 1.3–1.4 mHz. The first FLR (9 December 2001) is seen near the flank of the magnetosphere at high latitude. The second FLR (31 January 1997) has a very similar frequency and is observed roughly 2 hours prior to midnight, at approximately 5 degrees lower latitude. In both cases, the FLR is located on stretched geomagnetic field lines, with the envelope of the arc covering a perpendicular scale of 150 km or so in the 9 December 2001 observation and roughly 30 km or so in the 31 January 1997 observation. The high-latitude FLR is well represented by eigenmode analysis that accounts for field-line stretching

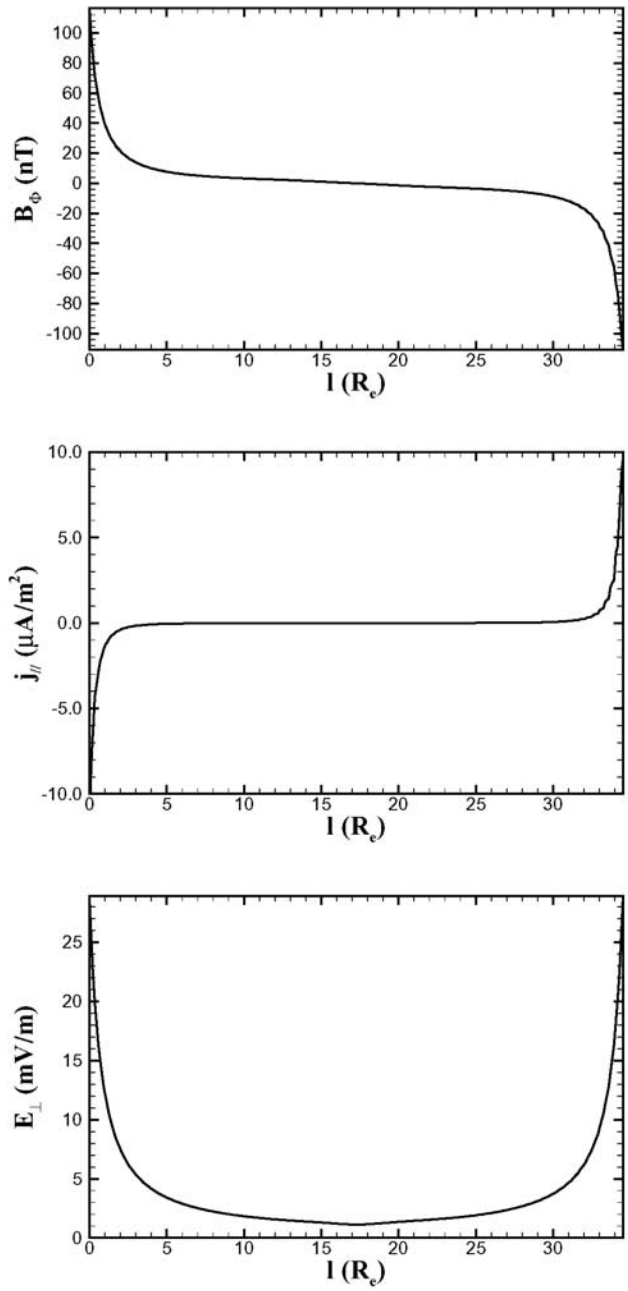

Figure 15. From top to bottom is shown the SAW azimuthal magnetic field, the field-aligned current, and the perpendicular electric field as a function of distance along the field line from one ionosphere to the other. The parameters of the field line are the same as in Figure 13.

and torsion or twisting of the geomagnetic field. In the lower latitude arc (31 January 1997), a rather high plasma sheet equatorial density is required to fit the eigenmode frequency. Here, we add a note of caution that our results are sensitive to field-line topology (which in both cases is represented by the approximate Tsyganenko 1996 magnetic field model), and it would be premature to conclude that plasma sheet densities are typically this high. A third example of FLRs (29 October 1998) that is intermediate between the two observations just described shows wave activity at frequencies between roughly 3.8 mHz and 5.2 mHz. This observation does not require high plasma sheet densities in order to fit the observed frequency. We find that our eigenmode analysis is able to explain how the frequency changes as a function of time in this example. In particular, the frequency variation over 1 hour of ULF wave activity is closely tracked by our model and analysis.

[28] Using the gradient in eigenfrequency computed from the Tsyganenko 1996 model and the equatorial plasma densities that are required to fit observed FLR frequencies, we have estimated the resulting spatial scale of FLR arcs that form. This relies on the calculation of the wave dispersion that is supported by the entire length of geomagnetic field lines. Using simple density profiles along the field line ($\propto 1/r$), and a reduced MHD envelope model of FLRs, we find that our estimates are in agreement with observed scales that range from a few tens of kilometers to around 150 km. Our estimates of the associated linear phase mixing times vary between 8 and 15 SAW periods, which is quite reasonable in the context of the lifetime of arcs observed in optical data for the events we have studied. We further demonstrate that FLRs can nonlinearly heat electrons, producing significant changes in Pedersen conductance under the resonant field line on which SAWs naturally form. By incorporating nonlinear electron heating into the boundary condition used in a 2-D reduced MHD dispersive MHD code we show that strong Pedersen conductivity gradients act to strongly localize FLRs in latitude, in agreement with a substantial number of observations.

[29] In future work, we hope to combine our reduced MHD and nonlinear electron heating model of SAWs with nonlinear effects that steepen the local Alfvén speed gradient. It has been shown that SAW ponderomotive forces can produce highly structured FLRs that are strongly localized in latitude. In this situation, dispersive waves with perpendicular scale sizes comparable to the electron inertial or ion gyroradius are expected to form. This is necessary to explain electron acceleration through parallel electric fields that are excited in association with highly localized field-line resonances. Finally, our analysis has not considered the parallel electric fields associated with dispersive SAWs. It has been shown that this requires kinetic effects which are outside the scope of MHD models. The reader is referred to *Rankin et al.* [1999b], *Tikhonchuk and Rankin* [2002], *Lysak and Song* [2003], and *Wright et al.* [2002] for a description of particular models of kinetic effects involving dispersive scale SAWs.

[30] **Acknowledgments.** This research was supported by the Natural Sciences and Engineering Research Council of Canada and the Canadian Space Agency.

[31] Shadia Rifai Habbal thanks Robert Louis Lysak and another referee for their assistance in evaluating this paper.

References

Akasofu, S.-I. (1974), A study of auroral displays photographed from the DMSP-2 satellite and from the Alaska meridian chain of stations, *Space Sci. Rev.*, *16*, 617.

Allan, W. (1995), Transient ULF pulsations: Time dependence of magnetic fields observed at the ground, *Ann. Geophys.*, *13*, 938.

Allan, W., and F. B. Knox (1979), The effect of finite ionosphere conductivities on axisymmetric toroidal Alfvén wave resonances, *Planet. Space. Sci.*, *27*, 939.

Beamish, D., H. Hanson, and D. Webb (1979), Complex demodulation applied to Pi2 geomagnetic pulsations, *Geophys. J. R. Astron. Soc.*, *58*, 471.

Borovsky, J. E. (1993), Auroral arc thickness as predicted by various theories, *J. Geophys. Res.*, *98*, 6101.

Carlson, C. W., R. F. Pfaff, and J. C. Watson (1998), The Fast Auroral Snapshot (FAST) mission, *Geophys. Res. Lett.*, *25*, 2013.

Chaston, C. C., C. W. Carlson, R. E. Ergun, J. P. McFadden, and R. J. Strangeway (2003), Properties of small-scale Alfvén waves and accelerated electrons from FAST, *J. Geophys. Res.*, *108*(A4), 8003, doi:10.1029/2002JA009420.

Chaston, C. C., et al. (2005), Energy deposition by Alfvén waves into the dayside auroral oval: Cluster and FAST observations, *J. Geophys. Res.*, *110*, A02211, doi:10.1029/2004JA010483.

Chen, L., and A. Hasegawa (1974), A theory of long period magnetic pulsations: 1. Steady state excitation of field-line resonance, *J. Geophys. Res.*, *79*, 1024.

Cheng, C. Z., and S. Zaharia (2003), Field-line resonances in quiet and disturbed time three-dimensional magnetospheres, *J. Geophys. Res.*, *108*(A1), 1002, doi:10.1029/2002JA009470.

Chui, Y. T., and M. Schultz (1978), Self-consistent particle and parallel electrostatic field distributions in the magnetospheric-ionospheric auroral regions, *J. Geophys. Res.*, *83*, 629.

Cummings, W. D., R. J. O'Sullivan, and P. J. Coleman Jr. (1969), Standing Alfvén waves in the magnetosphere, *J. Geophys. Res.*, *74*, 778.

D'haeseleer, W. D., W. N. G. Hitchon, J. D. Callen, and J. L. Shohet (1991), *Flux Coordinates and Magnetic Field Structure*, Springer, New York.

Farrugia, C. J., et al. (2000), Coordinated Wind, Interball/tail and ground observations of Kelvin-Helmholtz waves at the near-tail, equatorial magnetopause at dusk: January 11, 1997, *J. Geophys. Res.*, *105*, 7639.

Glassmeier, K.-H. (1995), ULF pulsations, in *Handbook of Atmospheric Electrodynamics*, part II, edited by H. Volland, pp. 463–502, CRC Press, Boca Raton, Fla.

Goertz, C. K. (1984), Kinetic Alfvén waves on auroral field lines, *Planet. Space Sci.*, *32*, 1387.

Hasegawa, A. (1976), Particle acceleration by MHD surface wave and formation of aurora, *J. Geophys. Res.*, *81*, 5083.

Keiling, A., J. R. Wygant, C. Cattell, M. Johnson, M. Temerin, F. Mozer, C. A. Kletzing, J. Scudder, C. T. Russell, and W. Peterson (2001), Properties of large electric fields in the plasma sheet at 4–7 R_E measured with Polar, *J. Geophys. Res.*, *106*, 5779.

Keiling, A., J. R. Wygant, C. Cattell, W. Peria, G. Parks, M. Temerin, F. S. Mozer, C. T. Russell, and C. A. Kletzing (2002), Correlation of Alfvén wave Poynting flux in the plasma sheet at 4–7 R_E with ionospheric electron energy flux, *J. Geophys. Res.*, *107*(A7), 1132, doi:10.1029/2001JA900140.

Kivelson, M. G., and D. J. Southwood (1986), Coupling of global magnetospheric MHD eigenmode to field-line resonances, *J. Geophys. Res.*, *91*, 4345.

Kletzing, C. A., and S. Hu (2001), Alfvén wave generated electron time dispersion, *Geophys. Res. Lett.*, *28*, 693.

Knight, S. (1973), Parallel electric field, *Planet. Space Sci.*, *21*, 741.

Knudsen, D. J., E. F. Donovan, L. L. Cogger, B. Jackel, and W. Shaw (2001), Width and structure of mesoscale optical arcs, *Geophys. Res. Lett.*, *28*, 3573.

Liu, W. W., B.-L. Xu, J. C. Samson, and G. Rostoker (1994), Theory and observation of auroral substorms: A magnetohydrodynamic approach, *J. Geophys. Res.*, *99*, 21,291.

Lotko, W., A. V. Streltsov, and C. W. Carlson (1998), Discrete auroral arc, electrostatic shock and suprathermal electrons powered by dispersive, anomalously resistive field-line resonance, *Geophys. Res. Lett.*, *25*, 4449.

Lu, J. Y., R. Rankin, R. Marchand, and V. T. Tikhonchuk (2003), Finite element modeling of nonlinear dispersive field-line resonances: Trapped shear Alfven waves inside nonlinear density perturbations, *J. Geophys. Res.*, *108*(A11), 1394, doi:10.1029/2003JA010035.

Lysak, R. L., and Y. Song (2003), Non-local kinetic theory of Alfvén waves on dipolar field lines, *J. Geophys. Res.*, *108*(A8), 1327, doi:10.1029/2003JA009859.

Maggs, J. E., and T. N. Davis (1968), Measurements of the thicknesses of auroral structures, *Planet. Space Sci.*, *16*, 205.

Mann, I. R., A. N. Wright, and P. S. Cally (1995), Coupling of magnetospheric cavity modes to field-line resonances: A study of resonance widths, *J. Geophys. Res.*, *100*, 19,441.

Marchand, R., and M. Simard (1997), Finite element modeling of TdeV edge and divertor with E × B drifts, *Nucl. Fusion*, *37*, 1629.

Prakash, M., R. Rankin, and V. T. Tikhonchuk (2003), Precipitation and nonlinear effects in geomagnetic field-line resonances, *J. Geophys. Res.*, *108*(A4), 8014, doi:10.1029/2002JA009383.

Proehl, J. A., W. Lotko, I. Kouznetsov, and S. D. Geimer (2002), Ultralow-frequency magnetohydrodynamic in boundary-constrained geomagnetic flux coordinates, *J. Geophys. Res.*, *107*(A9), 1225, doi:10.1029/2001JA000135.

Rae, I. J., K. Kabin, R. Rankin, F. R. Fenrich, W. Liu, J. A. Wanliss, A. J. Ridley, T. I. Gombosi, and D. L. DeZeeuw (2004), Comparison of photometer and global MHD determination of the open-closed field-line boundary, *J. Geophys. Res.*, *109*, A01204, doi:10.1029/2003JA009968.

Rankin, R., J. C. Samson, V. T. Tikhonchuk, and I. Voronkov (1999a), Auroral density fluctuations on dispersive field-line resonances, *J. Geophys. Res.*, *104*, 4399.

Rankin, R., J. C. Samson, and V. T. Tikhonchuk (1999b), Parallel electric fields in dispersive shear Alfvén waves in the dipolar magnetosphere, *Geophys. Res. Lett.*, *26*, 3601.

Rankin, R., F. Fenrich, and V. T. Tikhonchuk (2000), Shear Alfvén waves on stretched magnetic field lines near midnight in Earth's magnetosphere, *Geophys. Res. Lett.*, *27*, 3265.

Rankin, R., J. Y. Lu, R. Marchand, and E. F. Donovan (2004), Spatiotemporal characteristics of ultra-low frequency dispersive scale shear Alfvén waves in the Earth's magnetosphere, *Phys. Plasmas*, *11*, 1268.

Robinson, R. M., R. R. Vondrak, K. Miller, T. Dabbs, and D. Hardy (1987), On calculating ionospheric conductances from the flux and energy of precipitating electrons, *J. Geophys. Res.*, *92*, 2565.

Rostoker, G., J. C. Samson, F. Creutzberg, T. J. Hughes, D. R. McDiarmid, A. G. McNamara, A. Vallance Jones, D. D. Wallis, and L. L. Cogger (1995), CANOPUS – A ground based instrument array for remote sensing in the high latitude ionosphere during ISTP/GGS program, *Space Sci. Rev.*, *71*, 743.

Samson, J. C., J. A. Jacobs, and G. Rostoker (1971), Latitude dependent characteristics of long-period geomagnetic micropulsations, *J. Geophys. Res.*, *78*, 3675.

Samson, J. C., T. J. Hughes, F. Creutzberg, D. D. Wallis, R. A. Greenwald, and J. M. Ruohoniemi (1991), Observations of a detached, discrete arc in association with field-line resonances, *J. Geophys. Res.*, *96*, 15,683.

Samson, J. C., B. G. Harrold, J. M. Ruohoniemi, R. A. Greenwald, and A. D. M. Walker (1992), Field-line resonances associated with MHD waveguides in the magnetosphere, *Geophys. Res. Lett.*, *19*, 441.

Samson, J. C., R. Rankin, and V. Tikhonchuk (2003), Optical signatures of auroral arcs produced by field-line resonances; comparison with satellite observations and modeling, *Ann. Geophys.*, *21*, 933.

Singer, H. J., D. J. Southwood, R. J. Walker, and M. G. Kivelson (1981), Alfvén wave resonances in a realistic magnetospheric magnetic field geometry, *J. Geophys. Res.*, *86*, 4589.

Southwood, D. J. (1974), Some features of field-line resonances in the magnetosphere, *Planet. Space Sci.*, *22*, 483.

Streltsov, A. V., W. Lotko, A. Keiling, and J. R. Wygant (2002), Numerical modeling of Alfvén waves observed by the Polar spacecraft in the nightside plasma sheet boundary layer, *J. Geophys. Res.*, *107*(A8), 1173, doi:10.1029/2001JA000233.

Thompson, B. J., and R. L. Lysak (1996), Electron acceleration by inertial Alfvén waves, *J. Geophys. Res.*, *101*, 5359.

Tikhonchuk, V. T., and R. Rankin (2002), Parallel potential driven by a kinetic Alfvén wave on geomagnetic field lines, *J. Geophys. Res.*, *107*(A7), 1104, doi:10.1029/2001JA000231.

Tsyganenko, N. A., and D. P. Stern (1996), Modeling the global magnetic field of the large-scale Birkeland current systems, *J. Geophys. Res.*, *101*, 27,187.

Waters, C. L., J. C. Samson, and E. F. Donovan (1996), Variation of plasmatrough density derived from magnetospheric field-line resonances, *J. Geophys. Res.*, *101*, 24,787.

Wei, C. Q., J. C. Samson, R. Rankin, and P. Frycz (1994), Electron inertial effects on geomagnetic field-line resonances, *J. Geophys. Res.*, *99*, 11,265.

Wright, A. N., W. Allan, M. S. Rudermann, and R. C. Elphic (2002), The dynamics of current carriers in standing Alfvén waves: Parallel electric fields in the auroral acceleration region, *J. Geophys. Res.*, *107*(A7), 1120, doi:10.1029/2001JA900168.

E. F. Donovan, Department of Physics and Astronomy, University of Calgary, Calgary, Alberta, Canada.

K. Kabin, J. Y. Lu, I. R. Mann, R. Marchand, I. J. Rae, and R. Rankin, Department of Physics, University of Alberta, Edmonton, Alberta, Canada T6G 2J1. (rankin@space.ualberta.ca)

V. T. Tikhonchuk, Institut de Physique Fondamentale, Universite Bordeaux 1, B. P. 120, F-33175 Gradignan Cedex, France.